Check for updates

CLIMATOLOGY

Hemispheric asymmetry in evapotranspiration reveals terrestrial water-flux redistribution

Yongqiang Zhang[1]*, Congcong Li[1], Dongdong Kong[2], Zhenwu Xu[1], Diego Miralles[3], Tim R. McVicar[4], Jing Tian[1], Xuanze Zhang[1], Ning Ma[1], Xiaojie Li[1], Yongyong Zhang[1], Haoshan Wei[1], Gang Zhao[1], Jun Xia[5], Yuanyuan Huang[1], Zhipin Ai[1], Ronglin Tang[1], Ge Sun[6], Stefan Uhlenbrook[7], Georgia Destouni[8,9,10]

Copyright © 2026 The Authors, some rights reserved; exclusive licensee American Association for the Advancement of Science. No claim to original U.S. Government Works. Distributed under a Creative Commons Attribution NonCommercial License 4.0 (CC BY-NC).

Global warming is widely expected to intensify the hydrological cycle. However, observational evidence for accelerated evapotranspiration (ET), a key terrestrial water cycle and energy balance component, remains ambiguous. Here, we constrained diverse datasets using basin-scale ET estimates covering 47% of global land to reveal a hidden asymmetry. We found a small global change in ET [-0.06 ± 0.44 mm year^{-2} (millimeters per year squared), $P > 0.10$] from 2000 to 2022, resulting from strongly opposing hemispheric trends. The Northern Hemisphere shows noticeable ET increases (0.91 ± 0.46 mm year^{-2}, $P < 0.05$), primarily driven by vegetation greening, whereas the Southern Hemisphere exhibits strong declines (-2.63 ± 0.46 mm year^{-2}, $P < 0.05$) due to precipitation deficits. Our observation-constrained projections indicate that this asymmetry is likely to persist through 2050. The small global ET trend masks a marked compensation between northern greening and southern drying, suggesting that current models may overestimate homogenized water cycle intensification. Our study provides profound implications for global food security, carbon sequestration, drought risks, and regional climate adaptation.

INTRODUCTION

An intensification of the global water cycle is widely expected under climate change, with rising temperatures leading to increased evapotranspiration (ET), the critical process whereby water is transferred from the land (where it is in the liquid phase) to the atmosphere (where it is in the gas phase), controlling the large-scale terrestrial redistribution of water and energy, and ultimately altering patterns of water availability (*1*). While some studies show signs of this acceleration in historical records (*2*–*6*), regional ET trends remain inconsistent and poorly constrained (*3*, *7*–*10*). It is well recognized that existing ET products have large uncertainties due to the complex interplay of climatic and biophysical drivers that influence ET across spatial and temporal scales (*11*–*14*).

Among the key components of the terrestrial hydrological cycle—precipitation, ET, runoff, and water storage changes—ET is particularly challenging to quantify due to its invisible nature and high spatial-temporal variability (*11*, *15*), and the most uncertain (*16*). Over the past decade, extraordinary efforts have been made to improve understanding of global ET's magnitude, variability, and trends using eddy covariance flux network, remote sensing, land surface models, and reanalysis datasets (*3*, *14*, *17*–*24*). These approaches have advanced our ability to estimate ET locally, regionally, and globally, linking observed trends to global warming, land use and land cover changes, precipitation shifts, and climate variability and change. Machine learning and ensemble modeling techniques have furthered ET science and trend assessments by merging diverse datasets, reducing uncertainties (*25*–*27*), and determining how model area of applicability around the world depends on choices of acceptable error or uncertainty level (*28*). Despite these advancements, quantifying spatial and temporal ET patterns remains one of the most challenging tasks in global land hydrological studies. Direct comparison of various datasets for the same period (1980–2010) and land area coverage (*29*) shows greater dataset differences for global ET than precipitation and runoff. North-to-south hemispheric disparities in ET trends may also emerge because water availability shows large difference between the two hemispheres (*13*). However, the ET trends and hemisphere disparities remain poorly resolved and represent a critical uncertainty in projecting future water cycle intensification (*11*, *20*, *30*). Furthermore, emerging evidence suggests fundamental hemispheric asymmetries in other hydrological and climatic variables, such as water availability (*13*) and terrestrial water storage changes (*31*), raising the question of whether ET trends might also exhibit such a large-scale divergence.

To address this challenge, we developed an ensemble machine learning approach that integrates five diagnostic ET products with water-balance observational ET constructed using hydrometeorological observations from 183 large basins that cover about half of the global land area. The trained model was then applied to 232 globally distributed river basins (>10,000 km^2) from the HydroSHEDS dataset for full global and hemispheric analysis (see Materials and Methods). Unlike previous global ET assessments relying on simulation model output ensembles or remote sensing data alone or estimating ET from ground data for precipitation and streamflow, our framework uniquely harmonizes basin-scale water budgets (including also independent data for water storage changes) with machine learning techniques, resolving scale mismatches that have long obscured regional and global trends (see Materials and Methods). Our method demonstrates remarkable performance in simulating annual ET variability and trends (figs. S1 to S7 and table S3). Specifically, the

[1]Institute of Geographic Sciences and Natural Resources Research, Chinese Academy of Sciences, Beijing, China. [2]Department of Atmospheric Science, School of Environmental Studies, China University of Geosciences, Wuhan, China. [3]Department of Environment, Ghent University, Ghent, Belgium. [4]CSIRO Environment, Black Mountain, Canberra, Australia. [5]State Key Laboratory of Water Resources Engineering and Management, Wuhan University, Wuhan, China. [6]Eastern Forest Environmental Threat Assessment Center, USDA Forest Service, Research Triangle Park, NC, USA. [7]Federal Office of Meteorology and Climatology MeteoSwiss, Zürich, Switzerland. [8]Department of Physical Geography, Stockholm University, Stockholm, Sweden. [9]Department of Sustainable Development, Environmental Science and Engineering, KTH Royal Institute of Technology, Stockholm, Sweden. [10]Stellenbosch Institute for Advanced Study, Stellenbosch, South Africa.
*Corresponding author. Email: zhangyq@igsnrr.ac.cn

Downloaded from https://www.science.org at Digitop - USDA's Digital Desktop Library on October 06, 2026

prediction accuracy in our annual ET trends, indicated by the correlation coefficient (r), ranges from 0.82 to 0.90 during cross-validation, giving confidence in our results.

RESULTS

Global and hemispheric ET trends

From 2000 to 2022, the mean annual ET across the 232 river basins globally is estimated at 507.3 ± 6.14 mm year^{-1}, corresponding to a volumetric ET of ~(66.4 ± 0.80) × 10^3 km^3 year^{-1}, which is slightly lower than an independent global ET estimate (69.0 ± 6.2) × 10^3 km^3 year^{-1}, both not including Greenland and Antarctica (*32*). The highest ET values (>1000 mm year^{-1}) are observed in tropical river basins such as the Amazon, Congo, and Southeast Asian basins, whereas moderate values (500 to 1000 mm year^{-1}) are found in the Yangtze, Mississippi, Danube, and Rhine basins. In contrast, arid and semiarid regions, such as the Yellow River Basin, western United States, Sahara Desert, central Australia, central Asia, and the Arabian Peninsula, exhibit lower ET values (<500 mm year^{-1}; Fig. 1A).

Global ET experienced a nonsignificant trend of −0.06 ± 0.44 mm year^{-2} ($P > 0.05$) from 2000 to 2022 (Fig. 2). This is negligible over 23 years, despite large and opposing hemispheric changes, strongly

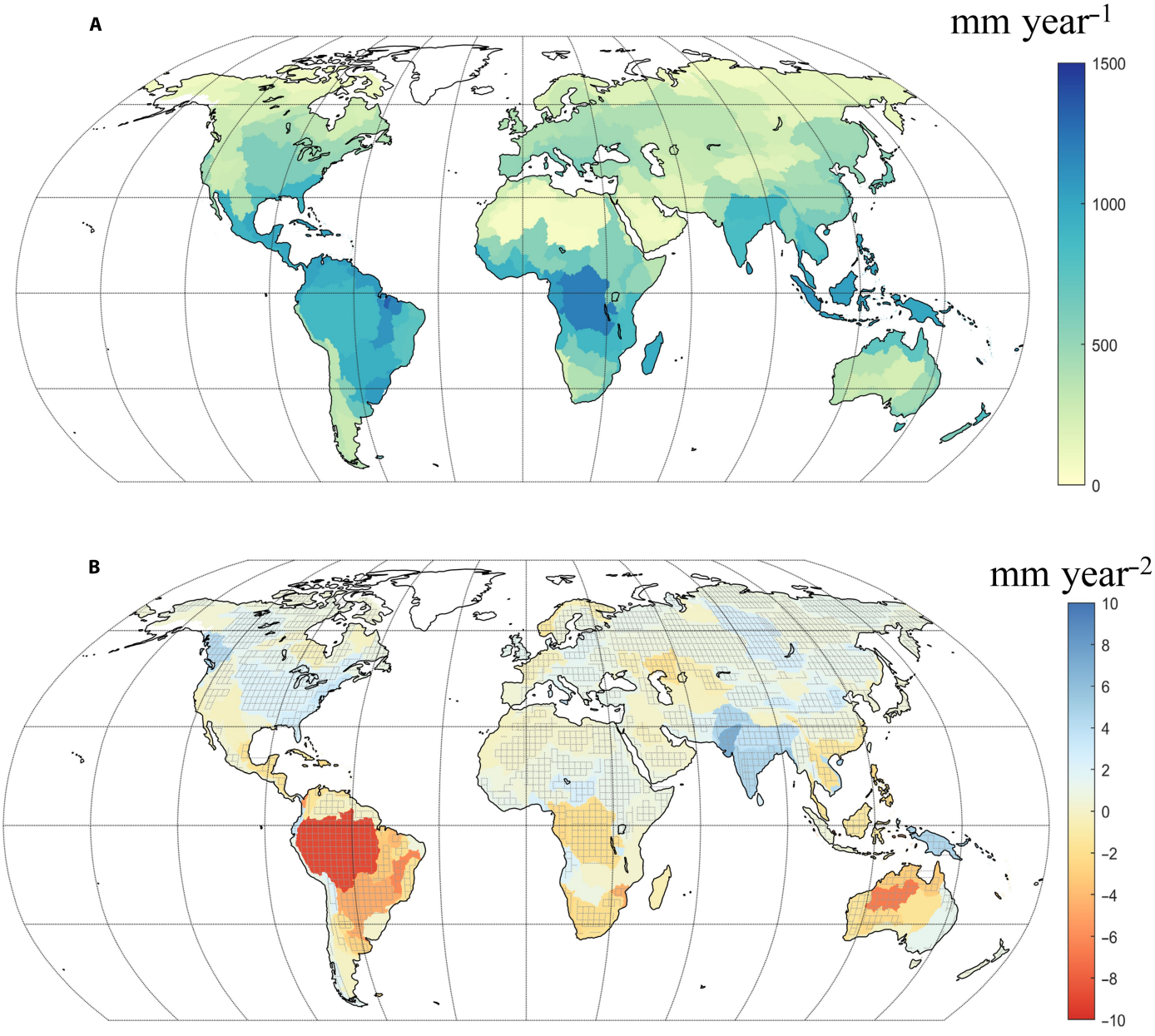


Fig. 1. Global ET mean and trend. Spatial pattern of mean annual ET in 2000–2022 for 232 river basins (>10,000 km^2) (**A**). The 232 simulation river basins are from HydroSHEDS level 3. Of the 232 basins used for global analysis, 173 are in the Northern Hemisphere and 59 in the Southern Hemisphere. Spatial pattern of annual ET trends over the same period and river basins (**B**). Cross-hatching denotes that the annual ET in the basins has significantly changed [$P < 0.05$, Mann-Kendall (MK) test]. Greenland and oceans are masked out.

Downloaded from https://www.science.org at Digitop - USDA's Digital Desktop Library on October 06, 2026

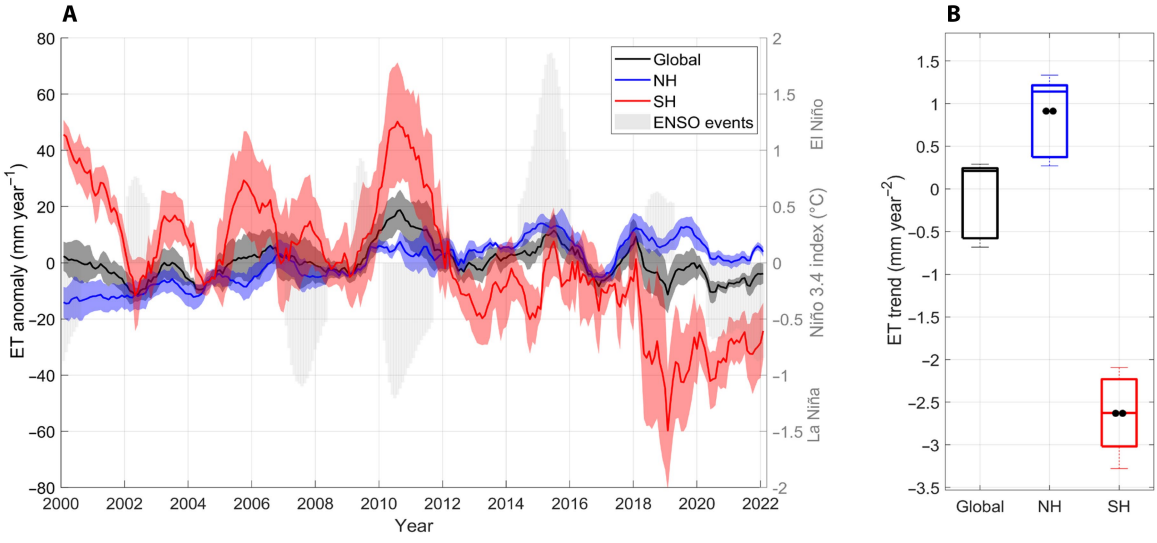


Fig. 2. Interannual variability in ET and its trend. Time series of ET anomaly across the globe, the Northern Hemisphere (NH), and the Southern Hemisphere (SH) for 2000 to 2022 (**A**). The El Niño–Southern Oscillation (ENSO) events are shown, with El Niño phase when the Nino 3.4 index exceeds 0.5°C for each 12 months and La Niña phase when the Nino 3.4 index falls below −0.5°C for each 12 months. Each thick line represents the ensemble mean of nine ET estimates and shading denotes ± one SD. ET trends for the globe, NH, and SH, respectively (**B**). The box-whisker plots are delineated using 10th, 25th, median, 75th, and 90th percentiles, respectively, from bottom to top in all three cases. Two dots in (B) denote the trend from the mean of the nine ET estimates with $P < 0.05$.

contrasting with reports of a 10% increase in a recently retracted article (*33*). Furthermore, this overall change conceals substantial hemispheric asymmetry. The Northern Hemisphere experienced a strong average ET increase of 0.91 ± 0.46 mm year^{-2} ($P < 0.05$), concentrated particularly in regions undergoing greening, whereas the Southern Hemisphere witnessed a strong average decline of -2.63 ± 0.46 mm year^{-2} ($P < 0.05$), primarily driven by declines in South America and Australia (Fig. 1B). The Amazon River basin accounted for more than 40% of the total trends in the Southern Hemisphere (fig. S12). Given the larger landmass (i.e., after excluding Greenland and Antarctica, about 72.6% of the global land area is north of the equator) and consequent higher ET volumes in the Northern Hemisphere, the global trend remains negligible, despite the strong decline over the Southern Hemisphere. This asymmetry demonstrates that recent water cycle change is fundamentally heterogeneous, which has driven large-scale terrestrial water-flux redistribution. Furthermore, the sensitivity of global ET change to global air temperature change from 2000 to 2022 is $-0.29 \pm 1.45\%$ °C^{-1}. This is far below Clausius-Clapeyron expectations of ~7% specific humidity increase per degree of warming and also below the expected change in precipitation per degree of warming (hydrological sensitivity) of 2 to 3% (*34*).

Climate drivers and attribution analysis

To better understand the major drivers for recent trends in ET, we perform large-scale (i.e., global or hemispherical or continental) causality analysis and local-scale (i.e., catchment-scale) attribution analysis. At a large scale, our analysis reveals that decadal ET trends are regulated by strong El Niño–Southern Oscillation (ENSO) events (defined by Niño 3.4 index anomalies of <−0.5°C for La Niña or >0.5°C for El Niño) (Fig. 2). Strong La Niña years corresponded with positive ET anomalies in the Southern Hemisphere, whereas El Niño events suppressed ET in the Southern Hemisphere. We further quantify the correlation between the Niño 3.4 index and annual ET anomalies during strong ENSO events (*35*). The analysis reveals contrasting hemispheric responses: Significant negative correlations ($P < 0.05$) dominated in the Southern Hemisphere, whereas positive correlations prevailed in the Northern Hemisphere. These opposing hemispheric effects result in a weakened global-scale signal. The markedly higher interannual variability in Southern Hemisphere ET (Fig. 2A) is likely driven by the greater influence of high-amplitude climate modes like ENSO on precipitation in the Southern Hemisphere, particularly in Australia (fig. S13), coupled with the larger proportion of water-limited ecosystems where ET variability closely tracks precipitation variability. Specifically, strong negative correlations between ENSO and ET emerge in southeastern/northern Australia and southern Africa. Notably, the Amazon basin exhibits weaker-than-expected impacts.

For attribution analysis, we identify factors including land surface conditions [e.g., leaf area index (LAI)] and atmospheric factors [e.g., precipitation and potential evapotranspiration (PET)] that directly affect and influence the ET trends (Fig. 3). Precipitation positively influences the ET trends in South America and Australia, with contribution reaching about 29 and 42%, respectively. PET, which integrates net radiation and other atmospheric drivers (Materials and Methods, Eq. 2), plays a dominant role in majority of high latitude basins (i.e., >50° from the equator) and large parts of the Southern Hemisphere (including Amazon basin), indicating the importance of energy limitation in these regions. The decrease in ET in Southern Hemisphere is largely dominated by decrease in precipitation, increase in PET, and its key driver of vapor pressure deficit (figs. S14 and S16). This interpretation is further supported by hemispheric-scale covariability in standardized annual anomalies (fig. S15), which shows a strong negative coupling between ET and air temperature in Northern Hemisphere ($r = 0.78$), but a negative coupling in Southern Hemisphere ($r = -0.62$), whereas ET-precipitation relationships are similar between hemispheres ($r = 0.65$ for Northern Hemisphere and $r = 0.66$ for Southern Hemisphere). In regions such as Europe and Asia, land cover changes contributed ~45% or more to the annual

Downloaded from https://www.science.org at Digitop - USDA's Digital Desktop Library on October 06, 2026

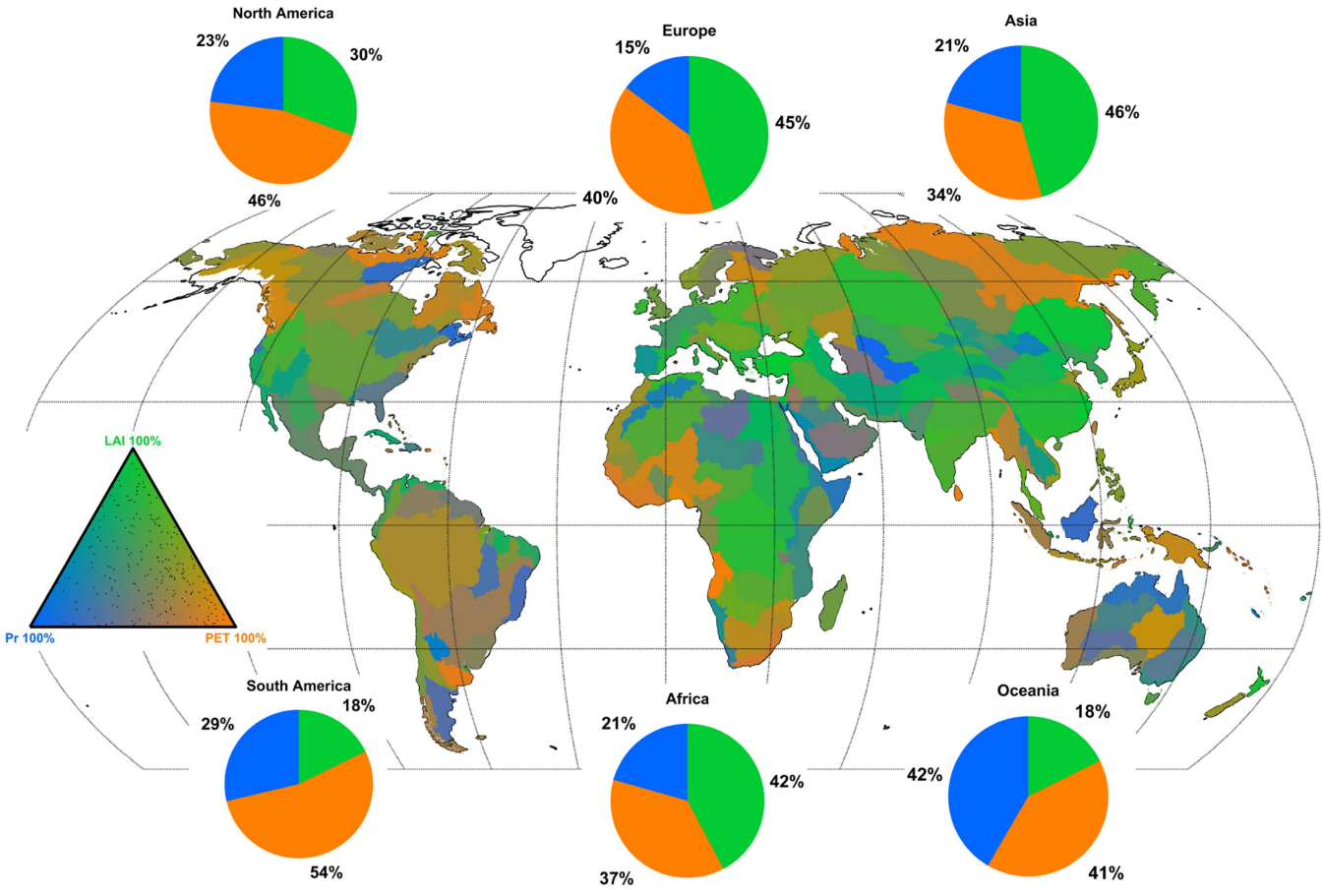


Fig. 3. Key contributing factors on ET trends across each river basin. Relative contributions (%) of precipitation (Pr), potential evapotranspiration (PET), and leaf area index (LAI) to the ET trends are estimated from the generalized additive model coupled with Shapley additive explanations (GAM-SHAP). The total contribution is 100%. The relative contribution of each driver (Pr, PET, and LAI) is indicated by dot position within the triangular legend and by color intensity in the map.

ET trends. This suggests that vegetation dynamics play a crucial role in Northern Hemisphere ET variations, and LAI in Northern Hemisphere is accompanied by strong greening, e.g., increase in LAI.

Future projection

To project future trends, we first evaluate 32 online Earth System Models (ESMs). Their ensemble average shows a similar ET global trend to our estimate for the same period (i.e., 2000–2022). However, most of them do not show notable contrasting signs in their hemispheric trends (table S1 and fig. S17). This stimulates us to reduce ESM uncertainty for better future ET projections. Using the emergent constraint framework that is widely used to reduce uncertainty for future projections (*23*, *36*–*38*), we establish robust relationships between historical trends and future changes (2025–2050 relative to 1981–2014) based on the results of ESMs in the Coupled Model Intercomparison Project Phase 6 (CMIP6) under a moderate Shared Socioeconomic Pathway 2-4.5 (SSP2-4.5) for the global land, the Northern Hemisphere, and the Southern Hemisphere (Fig. 4). Applying the emergent constraint (*23*, *36*–*38*) using the global ET trend only slightly changes the future projection of ET increase from the ESMs results. This is expected because our historical results are similar to the historical simulations of the ESMs ensemble. However, it is notable that, when the ESMs are constrained using hemispheric trend results, the future changes for both hemispheres are greatly altered. The constrained projected increase in the Northern Hemisphere is considerably larger than the raw projections; the constrained projected decrease in the Southern Hemisphere is substantially smaller than the raw projections. This suggests that the present asymmetric ET trends are likely to persist in the future. Our analysis indicates that the raw ensemble of ESMs tends to underestimate the magnitude of this future hemispheric asymmetry (Fig. 4). This underestimation implies that climate risk assessments based directly on ESM outputs may understate the divergence in hydrological futures. Water availability stress in the Southern Hemisphere is increasing while land-atmosphere coupling in the Northern Hemisphere is intensified with important consequences for adaptation planning. While we focus on the SSP2-4.5 scenario for consistency with a central, moderate pathway, future work could explore the sensitivity of this persistent asymmetry to other socioeconomic and emission scenarios.

DISCUSSION

Our findings provide a paradigm for the global intensification of the hydrological cycle under global warming (*1*, *39*, *40*). We demonstrate that the net increase in global terrestrial ET (2000–2022) masks a profound hemispheric asymmetry, with Northern Hemisphere greening

Downloaded from https://www.science.org at Digitop - USDA's Digital Desktop Library on October 06, 2026

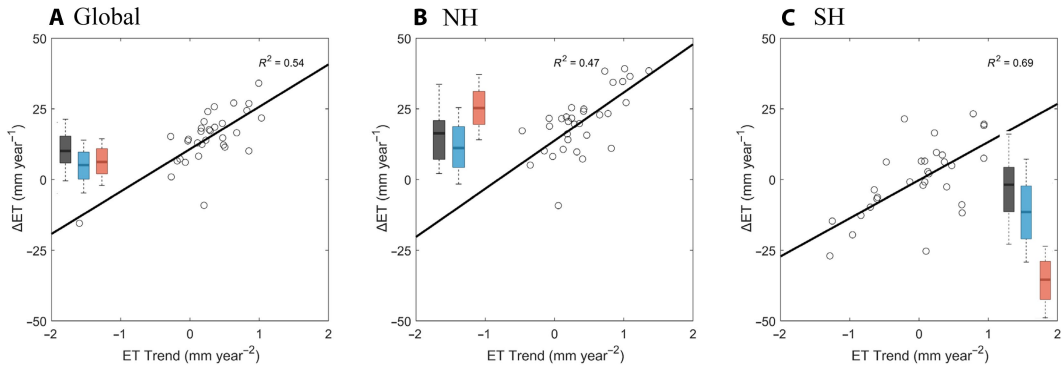


Fig. 4. Emergent constraints of ET change (△ET) between 2025–2050 and 1981–2014 using the ET trend in 2000–2022. The global land (**A**), the Northern Hemisphere (NH) (**B**), and the Southern Hemisphere (SH) (**C**). Each dot represents one CMIP6 ESM. Each box delineates △ET by the median (black), box (25th to 75th percentiles), and whiskers (10th and 90th percentiles). Dark gray is for the raw results generated by the 32 ESMs; blue denotes the emergent constraint results using the entire global ET trend in 2000–2022 obtained from this study; red is analogous to blue but using the hemispheric ET trends for the corresponding emergent constraint.

driving robust ET increases while the Southern Hemisphere exhibits significant declines (Fig. 2). The weak global mean trend arises from compensation between strong and opposing hemispheric responses, rather than from an absence of ET change. Such asymmetry is unexpected. In the Southern Hemisphere, the observed decline in ET contradicts the expected acceleration of the water cycle. We further demonstrate that contrasting regional forcings drive a hemispheric redistribution of water fluxes.

Our finding on low sensitivity of global ET change to global air temperature change indicates that terrestrial ET is only partially influenced by temperature-increased atmospheric demand but strongly constrained by moisture supply and vegetation physiology. This reinforces the paradigm that, over land, water availability, mediated by precipitation, plant responses, and land-atmosphere feedbacks, is the primary regulator of the hydrological cycle's intensification, tempering the influence of rising temperatures alone.

The increase in ET across the Northern Hemisphere aligns with widespread vegetation greening, notably due to afforestation in China and India (fig. S14) (*41*), where increasing LAI has contributed >50% of the ET trend (Fig. 3). In contrast, atmospheric evaporation demand (e.g., PET) has shown little change in these strongly greening regions because of compensation effects between increase in vapor pressure deficit and decreases in net radiation and wind speed (figs. S14 and S16). Conversely, the decline in the Southern Hemisphere primarily reflects precipitation deficits and complex atmospheric evaporation demand and land surface changes (fig. S14). Specifically, moisture supply to South America and central Australia has been suppressed over the past two decades, outweighing any radiation- or aerodynamically driven increases in evaporation potential. These contrasting hemispheric patterns are conceptualized in Fig. 5. Based on our projections (Fig. 4), these trends are likely to persist in the future.

Our results demonstrate that simple averaging of model outputs may introduce significant bias. Compared to our results, the five diagnostic ET models used here showed smaller hemispheric ET trend differences and overall overestimation of the global ET trend (fig. S17). This means that simple ensemble model output averaging would strongly underestimate hemispheric ET discrepancy. Furthermore, each of the five individual ET products exhibits lower correlations with the observed ET obtained from basin water balance (figs. S18 and S19). This demonstrates that it is necessary to process diagnostic results for better estimates of ET dynamics at the global and hemispheric scales. The failure of most ESMs to capture the contrasting hemispheric trends (table S1 and fig. S17) indicates the remaining structural limitations in representing vegetation-hydroclimate coupling (*42*, *43*). These may be related to underestimating the CO_2-fertilization feedback (*44*) and afforestation/reforestation impacts (*41*) on vegetation changes in the Northern Hemisphere. For the Southern Hemisphere and its more water-limited conditions (*29*), ESMs may underestimate ET declines from precipitation deficits (*45*) and additional ENSO-enhanced drying (Fig. 4) (*46*–*48*). Our emergent constraints project that this asymmetry will persist through 2050, implying that evaporation paradox (*49*, *50*) of decreasing ET in a warmer climate is not transient but a signature of hemispherically divergent water cycles.

The hemispheric asymmetries in ET trends have not only direct implications for global water cycle but also broader implications. The increased ET in the Northern Hemisphere not only may reflect enhanced vegetation growth, forest expansion, and carbon sequestration (*41*, *51*) but also implies higher agricultural water use, intensifying competition for freshwater resources under increased atmospheric demand for water. Conversely, the declining ET in the Southern Hemisphere due to atmospheric drying may be associated with lower crop yields, exacerbating food insecurity in water-scarce regions. The declining precipitation may also increase irrigation demand, which cannot always be met sustainably at local/regional scales, and also exacerbates water resource competition and requires significant infrastructure investments (*52*). This is particularly critical for southeast Australia and Brazil, both at the forefront of global food production. These trends also pose challenges for hydropower generation, ecosystem stability/integrity, and biodiversity conservation.

While our approach advances global ET estimates and trend analysis, certain considerations or clarifications should be noted. First, we account for precipitation uncertainty by using three state-of-the-art precipitation products. Nevertheless, precipitation uncertainty may remain substantial in regions with sparse gauge coverage (*53*). Despite this, all three products consistently revealed contrasting hemispheric patterns, with slight variations in magnitude due to the nature of our model, which is constrained by basin water balances and thus directly influenced by precipitation inputs (fig. S8). Second, our estimations are conducted at a basin scale (≥10,000 km^2), meaning that

Downloaded from https://www.science.org at Digitop - USDA's Digital Desktop Library on October 06, 2026

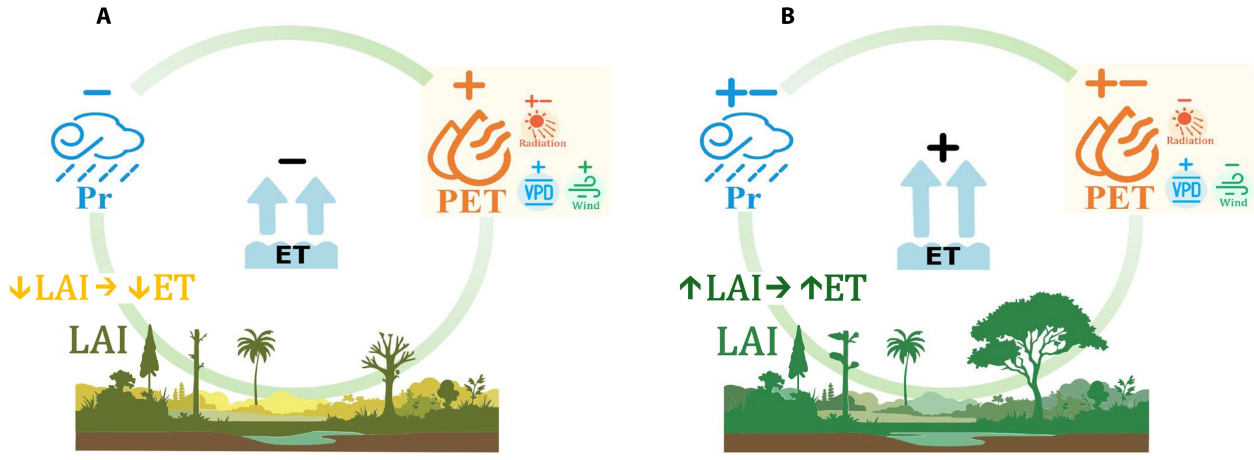


Fig. 5. Conceptualized understanding of ET impact mechanisms. They are demonstrated in two typical regions (Australia and China) in the Southern Hemisphere (**A**) and the Northern Hemisphere (**B**), respectively. Pr reflects water supply; PET indicates atmospheric evaporation demand primarily controlled by energy (net radiation) and water vapor transfer [vapor pressure deficit (VPD) and wind speed] drivers; LAI shows vegetation condition. The notations of "+ (or ↑)", "− (or ↓)", and "+−" denote the increasing trend, the decreasing trend, and the marginal change, respectively.

direct point-scale validation using flux tower data is not directly applicable, an inherent characteristic of basin-scale water-balance studies. However, these approaches are complementary: Basin-scale reconciliations provide a spatially integrated, mass-constrained benchmark, whereas flux towers offer mechanistic insights at fine temporal scales. Future studies could use this framework to integrate flux tower data with catchment streamflow and large-basin terrestrial water storage, providing robust constraints for refined water-flux estimates. Third, while our framework captures annual ET trends, it does not address seasonal and subseasonal variations; addressing these requires finer temporal scale study. Nevertheless, investigating short-term fluctuations driven by extreme weather events and vegetation changes is another important topic for future research. Fourth, the dominant drivers identified represent strong statistical associations derived from the generalized additive model coupled with Shapley additive explanations (GAM-SHAP) analysis. While these are consistent with well-established hydrological principles (e.g., ET limitation by P in dry regions and influence of LAI via transpiration), they indicate correlation and mechanistic plausibility rather than definitive causation. Fifth, we use moving averages for both the ET–water-balance model constraint and the GAM-SHAP analysis, which can introduce autocorrelation, influencing *P* values and regression diagnostics. This approach, however, offers a clear advantage by more effectively revealing the underlying low-frequency hydroclimatic trends compared to annual block averages, a well-established method for improving the signal-to-noise ratio in climate trend analysis (*54*, *55*).

By integrating machine learning with individual diagnostic ET products and basin-scale water-balance estimates, our approach provides a robust baseline for global ET trend assessments and projections, such as the annual report of World Meteorological Organization (WMO) State of Global Water Resources (*56*) and Intergovernmental Panel on Climate Change climate assessments (*34*). Together, these results show that recent changes in terrestrial ET are characterized by hemispheric redistribution rather than uniform global intensification, underscoring the importance of considering regional disparities in climate adaptation and water management strategies. Moving forward, incorporating data from improved observational networks, Earth observations, and advanced modeling techniques will be essential to refine global water cycle projections across spatiotemporal scales and ensure effective policy interventions. By reconciling hemispheric ET trends, this work supports achieving United Nation Sustainable Development Goal 6 (SDG 6; clean water and sanitation) and SDG 13 (climate action) through improved drought forecasting and refined climate projections.

MATERIALS AND METHODS

Basin water balance and datasets

Actual ET at a basin scale can be quantified using precipitation (Pr; millimeters per year), streamflow (*Q*; millimeters per year), and basin storage changes (Δ*S*; millimeters per year; integrated terrestrial water storages in soil moisture, groundwater, lakes, reservoirs, snow, and ice)

$$\mathrm{ET} = \mathrm{Pr} - \Delta S - Q \quad (1)$$

The water-balanced quantified ET at the basin scale is regarded as a "pseudo-observation" because Pr, *Q*, and Δ*S* can be all estimated on the basis of the ground measurements (Pr and *Q*) or satellite observations (Δ*S*). Pr and Δ*S* are obtained by area-weighted averaging of all 0.25° grid values within the basin; *Q* is obtained from the observations of basin outlet. In cases where water is transferred across basin boundaries, the monthly transferred volume is added to *Q* in the donor basin and subtracted from *Q* in the receiving basin. How the three water-balance components are obtained is detailed in the following.

Three state-of-the-art diagnostic Pr products were selected from 2000 to 2022 (276 months), including Climatic Research Unit (CRU) gridded Time Series (*57*), Multi-Source Weighted-Ensemble Precipitation (MSWEP) version 2 (*58*), and Global Precipitation Climatology Project (GPCP) version 3.2 (*59*). The CRU Pr is a widely used climate dataset on a 0.5° latitude by 0.5° longitude grid over all land domains of the world. MSWEP is a global precipitation product with a 3 hourly 0.1° resolution. The product merges with gauge, satellite, and reanalysis datasets. The GPCP dataset provides a gridded (level 3) homogeneously processed record of global precipitation estimates at 0.5° spatial and daily temporal resolution. Δ*S* data were obtained

Downloaded from https://www.science.org at Digitop - USDA's Digital Desktop Library on October 06, 2026

from three sources (*60*–*62*): (i) JPL Mascon RL06M.1 version 3; (ii) CSR RL06 Mascon version 2; and (iii) GSFC Mascon RL06 version 2. All datasets were generated using the Gravity Recovery and Climate Experiment (GRACE) satellites and their successor, GRACE Follow-on (GRACE-FO) satellites. This study used the Monthly Mass Grids - Global mascons with a 0.5° spatial resolution. There existed 11-month continuous and 24-month isolated GRACE data gaps during the transition between the two satellite missions from July 2017 to May 2018. For the missing data, we used an innovative transformer-based deep learning model for data gap-filling (*63*), which strongly improved Δ*S* gap filling in arid regions, indicated by 11.8 to 42.3% reductions in root mean square error, compared to traditional deep learning approaches (*64*, *65*). We acknowledge the signal leakage of GRACE data in small basins and conducted a comparison between the Δ*S* values obtained from the original and two state-of-the-art downscaled products (*66*, *67*). The results showed high consistency between the two, with a coefficient of determination (R^2) of 0.98 or higher (fig. S9). Furthermore, we tested the training and cross-validation results of our machine learning model derived from both Δ*S* datasets and found that using the downscaled Δ*S* did not yield noticeably better outcomes (figs. S10 and S11). Therefore, we used the Δ*S* results mentioned above for the remainder of the analysis.

For *Q* data, we used monthly streamflow data obtained from six sources: (i) the Global Runoff Data Centre (located in Germany; https://grdc.bafg.de/, last accessed 3 March 2025); (ii) the US Geological Survey National Water Information System and Geospatial Attributes of Gages for Evaluating Streamflow II database (www.usgs.gov/data/statistical-daily-streamflow-estimates-gages-ii-non-reference-streamgages-conterminous-united; last assessed 28 February 2025); (iii) the Australian Bureau of Meteorology (www.bom.gov.au/water/hrs/, last accessed 1 February 2025); (iv) the Chinese River Sediment Bulletin (www.irtces.org/nszx/cbw/hlnsgb/A550406index_1.htm, last accessed 25 November 2024); (v) the Mekong River Commission (www.mrcmekong.org/, last accessed 3 March 2025); and (vi) the CAWATERinfo dataset for Central Asian rivers (www.cawater-info.net/bd/index_e.htm, last accessed 1 March 2025). To meet our research requirements, we established two criteria to select high-quality streamflow data: (i) the river basin area is larger than 30,000 km^2 to minimize the uncertainty of the coarse resolution of GRACE data (*13*); (ii) there are not more than 13 months of observations missing in the period from January 2003 to December 2023 (table S2), making sure that there are at least two gap-free moving-average years used for model training; and (iii) the volume of water transferred across basins must be less than 2% of the mean annual runoff in both the donor and receiving basins. Consequently, the Colorado River basin was excluded from our analysis because more than 10% of its runoff was transferred out (*68*). In contrast, its two receiving basins, including the Mississippi River basin and the Rio Bravo basin, were retained as the transferred water from the Colorado River basin accounts for only 0.16 and 1.47% of their respective mean annual runoff. For the Yangtze River basin, water transferred out via the South-to-North Water Diversion Project was added to the observed streamflow at its outlet gauge in Eq. 1 (table S3). The receiving basin, the low Hai River basin, was not included in the analysis. Ultimately, we selected 183 large river basins for training the machine learning model, which accounted for 47.1% of global land area (excluding Greenland and Antarctica). The basin ranges from 30,665 to 4,702,291 km^2, with 10th, 50th, and 90th percentiles of 37,690, 84,381, and 843,262 km^2, respectively (fig. S1). Furthermore, there are 90% basins having more than 100 months data available.

We estimated basin ET at an annual time scale. We used the moving window approach to estimate the annual ET from January 2000 to January 2022. The January 2000 annual ET means the period of January 2000 to December 2000, the February 2000 annual ET means the period of February 2000 to January 2001, and so on to the end of the period being January 2022 to December 2022. Pr and *Q* were aggregated at each of the annual slots, whereas Δ*S* is calculated as the difference between terrestrial water storage of a given month in next year and that of the same given month in current year. For each basin, this monthly-moving aggregation method results in 265 annual ET times series, and it provides a more robust trend estimation due to the increased sample size, smoother trends, better statistical power, and reduced influence of anomalies (*69*), compared to the 23 annual ET time series obtained if using only calendar year aggregation.

In summary, we had three Pr products and three Δ*S* products, and, by using all combinations, we obtained nine water-balance annual ET observations that were then used respectively to train our machine learning model to obtain nine simulations at basin and global scales (figs. S5 to S7). In this way, uncertainty in water-balance ET estimates can be quantified using one SD of the nine estimates. This will reduce estimated biases and obtain more reliable trends.

Diagnostic ET products

To train the machine learning model, we selected five state-of-the-art diagnostic actual ET products from 2000 to 2022, including (i) Penman-Monteith-Leuning Evapotranspiration (PML_V2), PML_v2.1.8 (*19*); (ii) Moderate-resolution Imaging Spectroradiometer dataset (MODIS), MOD16A2 (*70*); (iii and iv) two versions of Global Land Evaporation Amsterdam Model dataset (GLEAM), GLEAM v3.8a (*71*) and GLEAM4.1a (*24*); and (v) the Complementary Relationship product CR (*72*). Selection of the five products was carefully considered on the basis of representation of dominant methodologies, spatiotemporal compatibility, regional and global performance, and data availability for the study period 2000–2022. PML_v2.1.8 is a biophysical model coupled to the gross primary production process based on stomatal conductance theory with 8-day and 500-m resolution. MOD16A2 is based on the Penman-Monteith Equation and calculates the canopy conductance using the semiempirical model including various constraining factors, also with 8-day and 500-m resolution. GLEAM v3.8a estimates actual ET using the Priestley and Taylor potential ET multiplied by a semiempirical function of evaporative stress, having daily and 0.25° resolution. GLEAM4.1a uses a Penman equation and a stress computation based on deep learning, having daily and 0.1° resolution. Unlike the previous four products driven by remote sensing data, the CR dataset was solely driven by routine meteorological data, including air and dew-point temperatures, wind speed, and net radiation, having monthly and 0.25° resolution. Because MOD16A and PML_v2.1.8 have much higher spatial resolution, compared to the other three, these two were first resampled into 0.25° by the nearest neighbor method. We also unified the temporal resolution to monthly by adding the ET of the daily and 8-day resolution products. To calculate basin-scale ET, area weighting was applied to each ET product.

CMIP6 ESM ET simulations

We also compared our ET trends with those of CMIP6 ESMs. There were 32 CMIP6 ESMs used (table S1; https://esgf-data.dkrz.de/, last accessed 18 November 2024). ET simulations (the variable "evspsbl") of historical and business-as-usual scenario (SSP245) ripf1 realization

Downloaded from https://www.science.org at Digitop - USDA's Digital Desktop Library on October 06, 2026

were used. Historical simulations end in 2014. SSP245 was used to extend the historical scenario to 2022 and used for future scenario analysis.

Basin boundary data

For the global basin-scale analysis, we used level 3 of the HydroSHEDS global basin boundary dataset (*73*, *74*), which is based on elevation data obtained in 2000 by NASA's Shuttle Radar Topography Mission. This dataset offers a suite of geo-referenced datasets (vector and raster) at various scales, including river networks, catchment boundaries, drainage directions, and flow accumulations. The level 3 dataset covers reasonably large basins, including a total of 275 basins. To ensure that the training the machine learning model could be appropriately extrapolated, we only selected basins that exceeded 10,000 km^2. As a result, 232 basins were retained for the final analysis. Note that the excluded 43 small basins (i.e., <10,000 km^2) only account for 0.075% of the HydroSHEDS global basins by area. It is noted that the 183 training basins were selected based on streamflow gauge availability and rigorous data quality criteria, whereas the 232 river basins globally used for global and hemispheric analysis were derived solely from HydroSHEDS. This distinction ensures that the training basins reflect observational constraints, whereas the HydroSHEDS basins provide comprehensive spatial coverage for global and hemispheric assessments.

Of the 232 basins used for global analysis, 173 are in the Northern Hemisphere and 59 in the Southern Hemisphere. While the number of basins differs between hemispheres, the area-weighted aggregation ensures that large basins (e.g., Amazon, Congo, and Murray-Darling) dominate the hemispheric signal. The robustness of the asymmetry is supported by the consistency of trends within each hemisphere (Fig. 1B) and their physical plausibility with observed driver trends (figs. S14 and S15).

Climate index data

To account for the influence of ENSO on global ET variability, we incorporated the monthly Nino 3.4 index into our analysis. The Nino 3.4 index is derived from sea surface temperature (SST) anomalies in the equatorial Pacific Ocean averaged over the region bounded by 5°N to 5°S and 170°W to 120°W. The Nino 3.4 dataset (*35*) for January 1870 to December 2024 was obtained from NOAA website (https://psl.noaa.gov/gcos_wgsp/Timeseries/Nino34/, last accessed 23 January 2025). Positive Nino 3.4 index values indicate El Niño conditions, characterized by warmer-than-average SSTs in this region, whereas negative values indicate La Niña conditions, characterized by cooler-than-average regional SSTs. The Nino 3.4 index was used to examine the relationship between ENSO phases and ET anomalies at global and hemispheric scales.

Machine learning model

We used a random forest (RF) ensemble learning approach to generate ET, which used the five diagnostic ET estimates as inputs and the water-balance–derived ET as the target variable, an approach widely used in global hydrology (*13*). Specifically, this process harmonizes basin-scale water budgets (Eq. 1) with gridded diagnostic ET products by leveraging the water-balance–derived ET as a physically constrained pseudo-observation target for training. The basin-scale water budget integrates ground and satellite observations of precipitation, streamflow, and terrestrial water storage changes to provide an independent, spatially aggregated ET estimate. This target is then reconciled with five gridded diagnostic ET products (PML_V2, MOD16A2, GLEAM v3.8a, and GLEAM4.1a, CR_v1), which offer high-resolution spatial patterns but lack direct observational constraints at basin scales. The RF model acts as a reconciliation framework, and the harmonization ensures that the final ET estimates are simultaneously consistent with basin-scale mass balance and gridded process representations.

The five diagnostic ET products as described above, basin centroid coordinates [x (longitude), y (latitude)], and basin area were integrated as predictors. Hyperparameter tuning was conducted through systematic grid testing of tree numbers (50, 100, 150, 200) and minimum leaf sizes (5, 10, 15, 20). Model performance was evaluated using fivefold cross-validation based on both the Nash-Sutcliffe Efficiency and the R^2, ensuring robustness in both variability and trend representation. The final model configuration (150 trees and minimum leaf size of 10) was selected because it consistently provided optimal and stable performance across all nine independent water-balance ET ensemble members (table S4), rather than being tuned to a single realization. The training, validation, and ensemble-weighted aggregation procedures are implemented explicitly in the modeling code, ensuring that the reported results are directly reproducible.

The model was trained on the 183 basins (fig. S1) to predict moving annual ET from February 2002 (where the GRACE terrestrial water storage data became available) to January 2022, as described previously, leveraging the spatial and temporal variability of the diagnostic ET products. Basin-specific trends were analyzed using Sen's slope for observed, calibrated, and validated ET. Model validation was carried out using fivefold cross-validation to assess robustness. This means that all the samples were randomly split into five groups, each one of the five groups was, in turn, left out for cross-validation with the other four groups used for training model. In this way, all the five groups were looped, and all the samples for the 183 basins were then used for cross-validation. The optimized RF model achieved high r values (reported between observed and simulated trends) and improved diagnostic ET accuracy, demonstrating effective integration of multisource ET data and geospatial attributes for large-scale hydrological modeling (figs. S2 to S7). The optimized RF model was lastly used for simulations in all large river basins across global land area (excluding Greenland and Antarctica), enabling a comprehensive analysis of global ET trends. Figure S20 summarizes data preparation, training, and simulation of the RF machine learning model for annual ET at a basin scale.

Attribution analysis

We explored three drivers for attribution analysis, including two atmospheric variables [(i) Pr (millimeters per year) and (ii) PET (millimeters per year)] and one land surface variable [LAI (unitless being square meters of green leaf per square meter of ground)]. These three drivers are key to influence ET changes because Pr, PET, and LAI represent water supply, water demand, land vegetation condition, respectively (*11*, *21*). The temporal resolution for the three drivers is the same as the simulated ET. Pr and PET were aggregated to annual scales. PET was calculated using Shuttleworth's simplification (*75*) of Penman 1948 Equation

$$\mathrm{PET} = \frac{\Delta}{\Delta+\gamma} R_n + \frac{\gamma}{\Delta+\gamma} \frac{6.43\left(1+0.536U_2\right)D}{\lambda} \quad (2)$$

where Δ is the slope of the saturation vapor pressure curve to air temperature (kilopascals per degree Celsius), γ is the psychrometric constant

Downloaded from https://www.science.org at Digitop - USDA's Digital Desktop Library on October 06, 2026

(kilopascals per degree Celsius), R_n is net radiation (millimeters per day), λ is the latent heat of vaporization (megajoules per kilogram), U_2 is wind speed at 2-m height (meters per second), and D is vapor pressure deficit (kilopascals).

The input data for calculating PET include incoming solar radiation, incoming longwave radiation, vapor pressured deficit, wind speed, and air temperature that were generated from GLDAS-2.1 product (*76*) and albedo. The albedo and LAI time series data were obtained from the MODIS MCD43A3 and MOD15A2H products, respectively. Before their use, the raw albedo time series were gap filled by linear interpolation, whereas LAI time series were smoothed by Google Earth Engine Whittaker smoother (*77*). To address uncertainty, three precipitation products (CRU, GPCP, and MSWEP) were averaged and then analyzed with other drivers for the final attribution. Model performance was assessed using basin-specific R^2 values (fig. S21). In 95% of the 232 river basins, the three variables explain more than 87% of ET anomalies in 2000–2022, demonstrating robustness of our method.

We quantified contributions of the three drivers to global ET trends using a generalized additive model (GAM) (*78*) coupled with Shapley additive explanations (SHAP) (*28*, *79*, *80*). The approach of GAM coupled with SHAP ensures an interpretable decomposition of the ET response to individual predictors while accounting for nonlinear dependencies. Before applying the GAM and SHAP, we first standardized all inputs ($X_i^{\text{norm}}, i = 1, 2, \cdots, 8$) and ET ($\text{ET}^{\text{norm}}$) time series using

$$X_i^{\text{norm}} = \frac{X_i - \mu_{X_i}}{\sigma_{X_i}}, \text{and } \text{ET}^{\text{norm}} = \frac{\text{ET} - \mu_{\text{ET}}}{\sigma_{\text{ET}}} \tag{3}$$

where μ_{X_i} and μ_{ET} are the long-term means of driver X_i and ET, respectively; σ_{X_i} and σ_{ET} are the SD of driver X_i and ET, respectively; and n is the total number of inputs. This normalization ensures that all variables are dimensionless, improving stability of the following analysis. We then applied for a collinear screening to ensure the reliability and interpretability of our results. For the collinearity analysis, the variance inflation factor (VIF) for all drivers at the basin scale was calculated (*81*). Drivers with VIF > 5 were removed and all retained variables satisfied VIF < 5. If there is only one driver remaining after VIF filtering, then the two drivers with the highest interannual variances were selected to ensure robustness in attribution.

After these two processes, we implemented GAM and SHAP analysis. In the GAM model, annual ET is taken as a function of multiple climate and land surface predictors

$$\widehat{\text{ET}} = \beta_0 + \sum_{i=1}^{n} f_i(X_i) + \varepsilon \tag{4}$$

where $\widehat{\text{ET}}$ is the predicted annual ET for a basin, $f_i(\cdot)$ represents the smooth function of predictor X_i (e.g., T_a and LAI), β_0 is the intercept term, ε is the residual error, and n is the total number of predictors (e.g., three used here).

SHAP values ϕ_i provide a game-theoretic estimate of each predictor's impact

$$\widehat{\text{ET}} = \phi_0 + \sum_{i=1}^{n} \phi_i \tag{5}$$

where ϕ_i represents the contribution of driver X_i to $\widehat{\text{ET}}$ and ϕ_0 is the baseline ET prediction. To analyze long-term trends, we calculated SHAP values obtained using the moving annual window and for each predictor X_i.

To determine trends of the SHAP values, we apply Sen's slope estimator to the time series of moving annual SHAP values

$$S_i = \text{mean}\left(\frac{\phi_{i,t_2} - \phi_{i,t_1}}{t_2 - t_1}\right), \forall t_1 < t_2 \tag{6}$$

where S_i represents the trend of SHAP values for driver X_i and t_2 and t_1 are two consecutive time points with $t_2 - t_1$ representing the time interval (e.g., 1 month) between them. The relative contribution C_i of each driver is lastly computed as

$$C_i = \frac{|S_i|}{\sum_{i=1}^{n} |S_i|} \times 100\% \tag{7}$$

This formulation ensures that the dominant drivers of ET are identified on the basis of their contribution to long-term ET trends.

Emergent constraint approach

We used the emergent constraint framework, a widely used approach in Earth sciences (*23*, *36*–*38*), to reduce uncertainties in future projections of ET. This approach leverages the relationship between observable short-term trends (2000–2022) and long-term future changes (2025–2050 relative to 1980–2014) across an ensemble of ESMs. The underlying physical basis for this constraint is that models exhibiting realistic historical ET trends are more likely to produce reliable future projections.

For each ESM, we calculated hemispheric and global ET trends during 2000–2022 using Sen's slope estimator. These trends served as the predictor variable (x), whereas the corresponding future ET changes (ΔET) represented the predictand (y). A linear regression model $y = \beta_0 + \beta_1 x$ was fitted to the ESM ensemble. Observed ET trends ($x_{\text{obs}} \pm 1\ \text{SD}_{\text{obs}}$) were then used to constrain future ΔET projections through the relationship

$$\hat{y} = \beta_0 + \beta_1 x_{\text{obs}} \tag{8}$$

with total uncertainty $\varepsilon_y = \sqrt{(\text{SD}_{\text{obs}}{}^2 + \text{RMSE}^2)}$, where RMSE is the regression root mean square error from ESM-output relationship. The reasoning for Eq. 8 is that the SD generated from observation-constrained trend in historical period of 2000–2022 is independent from the error produced from ESMs scatter plotting (*23*). Therefore, their total uncertainty can be combined by SD_{obs} and RMSE (*82*).

ENSO's influence on ET anomalies

We quantified ENSO's impact on ET anomalies using the Niño 3.4 index (2000–2022) (*35*). Strong ENSO events were included (|Niño 3.4| > 0.5). Pearson correlations were used to identify the relationship between ENSO and annual ET after anomaly calculation at basin and hemispheric scales.

Trend analysis and significance test

For all trends analysis here, we applied the Sen's slope estimator and the Mann-Kendall (MK) test. Sen's slope provides a robust estimate of the trend magnitude, whereas the MK test evaluates the statistical significance of the trend. Trends were classified as increasing, decreasing, or no trend based on the slope direction and significance

Downloaded from https://www.science.org at Digitop - USDA's Digital Desktop Library on October 06, 2026

levels ($P < 0.05$). We used the "mean" instead of the "median" in Eq. 6 to estimate trends, ensuring that the trends are mathematically balanced, that is, the sum of area-weighted hemispheric ET trends equals the global trend.

Supplementary Materials

This PDF file includes:

Supplementary Text
Figs. S1 to S21
Tables S1 to S4

REFERENCES

1. Intergovernmental Panel on Climate Change (IPCC), in *Climate Change 2021 – The Physical Science Basis: Working Group I Contribution to the Sixth Assessment Report of the Intergovernmental Panel on Climate Change*, IPCC, Ed. (Cambridge Univ. Press, 2023), pp. 1055–1210.
2. C. H. Akhoudas, J.-B. Sallee, G. Reverdin, F. A. Haumann, E. Pauthenet, C. C. Chapman, F. Margirier, C. Lo Monaco, N. Metzl, J. Meilland, C. Stranne, Isotopic evidence for an intensified hydrological cycle in the Indian sector of the Southern Ocean. *Nat. Commun.* **14**, 2763 (2023).
3. X. Chen, L. Yuan, Y. Ma, D. Chen, Z. Su, D. Cao, A doubled increasing trend of evapotranspiration on the Tibetan Plateau. *Sci. Bull.* **69**, 1980–1990 (2024).
4. N. Ma, Y. Zhang, Increasing Tibetan Plateau terrestrial evapotranspiration primarily driven by precipitation. *Agric. For. Meteorol.* **317**, 108887 (2022).
5. V. B. P. Chagas, P. L. B. Chaffe, G. Bloeschl, Climate and land management accelerate the Brazilian water cycle. *Nat. Commun.* **13**, 5136 (2022).
6. P. J. Durack, S. E. Wijffels, R. J. Matear, Ocean salinities reveal strong global water cycle intensification during 1950 to 2000. *Science* **336**, 455–458 (2012).
7. L. Zuo, L. Zou, J. Xia, L. Zhang, H. Cao, D. She, Multi-scale analysis of six evapotranspiration products across China: Accuracy, uncertainty and spatiotemporal pattern. *J. Hydrol.* **650**, 132516 (2025).
8. R. Wartenburger, S. I. Seneviratne, M. Hirschi, J. Chang, P. Ciais, D. Deryng, J. Elliott, C. Folberth, S. N. Gosling, L. Gudmundsson, A.-J. Henrot, T. Hickler, A. Ito, N. Khabarov, H. Kim, G. Leng, J. Liu, X. Liu, Y. Masaki, C. Morfopoulos, C. Müller, H. M. Schmied, K. Nishina, R. Orth, Y. Pokhrel, T. A. M. Pugh, Y. Satoh, S. Schaphoff, E. Schmid, J. Sheffield, T. Stacke, J. Steinkamp, Q. Tang, W. Thiery, Y. Wada, X. Wang, G. P. Weedon, H. Yang, T. Zhou, Evapotranspiration simulations in ISIMIP2a—Evaluation of spatio-temporal characteristics with a comprehensive ensemble of independent datasets. *Environ. Res. Lett.* **13**, 075001 (2018).
9. Z. Cui, Y. Zhang, A. Wang, J. Wu, C. Li, Uncertainty analysis and data fusion of multi-source land evapotranspiration products based on the TCH Method. *Remote Sens.* **16**, 28 (2024).
10. M. A. Pascolini-Campbell, J. T. Reager, J. B. Fisher, GRACE-based mass conservation as a validation target for basin-scale evapotranspiration in the contiguous United States. *Water Resour. Res.* **56**, e2019WR026594 (2020).
11. Y. Yang, M. L. Roderick, H. Guo, D. G. Miralles, L. Zhang, S. Fatichi, X. Luo, Y. Zhang, T. R. McVicar, Z. Tu, T. F. Keenan, J. B. Fisher, R. Gan, X. Zhang, S. Piao, B. Zhang, D. Yang, Evapotranspiration on a greening Earth. *Nat. Rev. Earth Environ.* **4**, 626–641 (2023).
12. X. Lian, W. Zhao, P. Gentine, Recent global decline in rainfall interception loss due to altered rainfall regimes. *Nat. Commun.* **13**, 7642 (2022).
13. Y. Zhang, C. Li, F. H. S. Chiew, D. A. Post, X. Zhang, N. Ma, J. Tian, D. Kong, L. R. Leung, Q. Yu, J. Shi, C. Liu, Southern Hemisphere dominates recent decline in global water availability. *Science* **382**, 579–584 (2023).
14. W. Nie, S. V. Kumar, A. Getirana, L. Zhao, M. L. Wrzesien, G. Konapala, S. K. Ahmad, K. A. Locke, T. R. Holmes, B. D. Loomis, M. Rodell, Nonstationarity in the global terrestrial water cycle and its interlinkages in the Anthropocene. *Proc. Natl. Acad. Sci. U.S.A.* **121**, e2403707121 (2024).
15. K. Wang, R. E. Dickinson, A review of global terrestrial evapotranspiration: Observation, modeling, climatology, and climatic variability. *Rev. Geophys.* **50**, RG2005 (2012).
16. W. Dorigo, S. Dietrich, F. Aires, L. Brocca, S. Carter, J.-F. Cretaux, D. Dunkerley, H. Enomoto, R. Forsberg, A. Güntner, M. I. Hegglin, R. Hollmann, D. F. Hurst, J. A. Johannessen, C. Kummerow, T. Lee, K. Luojus, U. Looser, D. G. Miralles, V. Pellet, T. Recknagel, C. R. Vargas, U. Schneider, P. Schoeneich, M. Schröder, N. Tapper, V. Vuglinsky, W. Wagner, L. Yu, L. Zappa, M. Zemp, V. Aich, Closing the water cycle from observations across scales: Where do we stand? *Bull. Amer. Meteorol. Soc.* **102**, E1897–E1935 (2021).
17. J. Szilagyi, Y. Zhang, N. Ma, R. D. Crago, R. J. Qualls, J. Jozsa, Diminishing control of evaporation on rising land surface temperature of the Earth. *Commun. Earth Environ.* **5**, 613 (2024).
18. S. Pan, N. Pan, H. Tian, P. Friedlingstein, S. Sitch, H. Shi, V. K. Arora, V. Haverd, A. K. Jain, E. Kato, S. Lienert, D. Lombardozzi, J. E. M. S. Nabel, C. Otte, B. Poulter, S. Zaehle, S. W. Running, Evaluation of global terrestrial evapotranspiration using state-of-the-art approaches in remote sensing, machine learning and land surface modeling. *Hydrol. Earth Syst. Sci.* **24**, 1485–1509 (2020).
19. Y. Zhang, D. Kong, R. Gan, F. H. S. Chiew, T. R. McVicar, Q. Zhang, Y. Yang, Coupled estimation of 500 m and 8-day resolution global evapotranspiration and gross primary production in 2002-2017. *Remote Sens. Environ.* **222**, 165–182 (2019).
20. D. G. Miralles, M. J. van den Berg, J. H. Gash, R. M. Parinussa, R. A. M. de Jeu, H. E. Beck, T. R. H. Holmes, C. Jimenez, N. E. C. Verhoest, W. A. Dorigo, A. J. Teuling, A. J. Dolman, El Niño-La Niña cycle and recent trends in continental evaporation. *Nat. Clim. Chang.* **4**, 122–126 (2014).
21. Y. Zhang, J. L. Pena-Arancibia, T. R. McVicar, F. H. S. Chiew, J. Vaze, C. Liu, X. Lu, H. Zheng, Y. Wang, Y. Y. Liu, D. G. Miralles, M. Pan, Multi-decadal trends in global terrestrial evapotranspiration and its components. *Sci. Rep.* **6**, 19124 (2016).
22. K. Zhang, J. S. Kimball, R. R. Nemani, S. W. Running, Y. Hong, J. J. Gourley, Z. Yu, Vegetation greening and climate change promote multidecadal rises of global land evapotranspiration. *Sci. Rep.* **5**, 15956 (2015).
23. X. Lian, S. Piao, C. Huntingford, Y. Li, Z. Zeng, X. Wang, P. Ciais, T. R. McVicar, S. Peng, C. Ottle, H. Yang, Y. Yang, Y. Zhang, T. Wang, Partitioning global land evapotranspiration using CMIP5 models constrained by observations. *Nat. Clim. Chang.* **8**, 640–646 (2018).
24. D. G. Miralles, O. Bonte, A. Koppa, O. M. Baez-Villanueva, E. Tronquo, F. Zhong, H. E. Beck, P. Hulsman, W. Dorigo, N. E. C. Verhoest, S. Haghdoost, GLEAM4: Global land evaporation and soil moisture dataset at 0.1 resolution from 1980 to near present. *Sci. Data* **12**, 416 (2025).
25. M. Jung, S. Koirala, U. Weber, K. Ichii, F. Gans, G. Camps-Valls, D. Papale, C. Schwalm, G. Tramontana, M. Reichstein, The FLUXCOM ensemble of global land-atmosphere energy fluxes. *Sci. Data* **6**, 74 (2019).
26. A. Koppa, D. Rains, P. Hulsman, R. Poyatos, D. G. Miralles, A deep learning-based hybrid model of global terrestrial evaporation. *Nat. Commun.* **13**, 1912 (2022).
27. G. Forzieri, D. G. Miralles, P. Ciais, R. Alkama, Y. Ryu, G. Duveiller, K. Zhang, E. Robertson, M. Kautz, B. Martens, C. Jiang, A. Arneth, G. Georgievski, W. Li, G. Ceccherini, P. Anthoni, P. Lawrence, A. Wiltshire, J. Pongratz, S. Piao, S. Sitch, D. S. Goll, V. K. Arora, S. Lienert, D. Lombardozzi, E. Kato, J. E. M. S. Nabel, H. Tian, P. Friedlingstein, A. Cescatti, Increased control of vegetation on global terrestrial energy fluxes. *Nat. Clim. Chang.* **10**, 356–362 (2020).
28. D. Althoff, G. Destouni, Global patterns in water flux partitioning: Irrigated and rainfed agriculture drives asymmetrical flux to vegetation over runoff. *One Earth* **6**, 1246–1257 (2023).
29. M. Zarei, G. Destouni, A global multi catchment and multi dataset synthesis for water fluxes and storage changes on land. *Sci. Data* **11**, 1333 (2024).
30. M. Jung, M. Reichstein, P. Ciais, S. I. Seneviratne, J. Sheffield, M. L. Goulden, G. Bonan, A. Cescatti, J. Chen, R. de Jeu, A. J. Dolman, W. Eugster, D. Gerten, D. Gianelle, N. Gobron, J. Heinke, J. Kimball, B. E. Law, L. Montagnani, Q. Mu, B. Mueller, K. Oleson, D. Papale, A. D. Richardson, O. Roupsard, S. Running, E. Tomelleri, N. Viovy, U. Weber, C. Williams, E. Wood, S. Zaehle, K. Zhang, Recent decline in the global land evapotranspiration trend due to limited moisture supply. *Nature* **467**, 951–954 (2010).
31. B. Li, M. Rodell, Terrestrial water storage in 2023. *Nat. Rev. Earth Environ.* **5**, 247–249 (2024).
32. Y. Zhang, G. Blöschl, H. Wei, D. Kong, N. Ma, T. Wagener, J. Tian, J. Xia, C. Li, L. Wang, F. H. S. Chiew, L. R. Leung, X. Liu, H. Zheng, X. Zhang, C. Liu, Overestimation of past and future increases in global river flow by Earth system models. *Nat. Geosci.* **19**, 311–316 (2026).
33. M. Pascolini-Campbell, J. T. Reager, H. A. Chandanpurkar, M. Rodell, RETRACTED ARTICLE: A 10 per cent increase in global land evapotranspiration from 2003 to 2019. *Nature* **593**, 543–547 (2021).
34. H. Douville, K. Raghavan, J. Renwick, R. P. Allan, P. A. Arias, M. Barlow, R. Cerezo-Mota, A. Cherchi, T. Y. Gan, J. Gergis, D. Jiang, A. Khan, W. Pokam Mba, D. Rosenfeld, J. Tierney, O. Zolina, in *Climate Change 2021: The Physical Science Basis. Contribution of Working Group I to the Sixth Assessment Report of the Intergovernmental Panel on Climate Change*, V. Masson-Delmotte, P. Zhai, A. Pirani, S. L. Connors, C. Péan, S. Berger, N. Caud, Y. Chen, L. Goldfarb, M. I. Gomis, M. Huang, K. Leitzell, E. Lonnoy, J. B. Matthews, T. Maycock, T. Waterfield, O. Yelekçi, R. Yu, B. Zhou, Eds. (Cambridge Univ. Press, 2021), pp. 1055–1210.
35. N. A. Rayner, D. E. Parker, E. B. Horton, C. K. Folland, L. V. Alexander, D. P. Rowell, E. C. Kent, A. Kaplan, Global analyses of sea surface temperature, sea ice, and night marine air temperature since the late nineteenth century. *J. Geophys. Res. Atmos.* **108**, 4407 (2003).
36. P. M. Cox, C. Huntingford, M. S. Williamson, Emergent constraint on equilibrium climate sensitivity from global temperature variability. *Nature* **553**, 319–322 (2018).
37. P. M. Cox, D. Pearson, B. B. Booth, P. Friedlingstein, C. Huntingford, C. D. Jones, C. M. Luke, Sensitivity of tropical carbon to climate change constrained by carbon dioxide variability. *Nature* **494**, 341–344 (2013).
38. I. Y. Petrova, D. G. Miralles, F. Brient, M. G. Donat, S.-K. Min, Y.-H. Kim, M. Bador, Observation-constrained projections reveal longer-than-expected dry spells. *Nature* **633**, 594–600 (2024).

Downloaded from https://www.science.org at Digitop - USDA's Digital Desktop Library on October 06, 2026

39. T. G. Huntington, Evidence for intensification of the global water cycle: Review and synthesis. *J. Hydrol.* **319**, 83–95 (2006).
40. I. M. Held, B. J. Soden, Robust responses of the hydrological cycle to global warming. *J. Climate* **19**, 5686–5699 (2006).
41. C. Chen, T. Park, X. Wang, S. Piao, B. Xu, R. K. Chaturvedi, R. Fuchs, V. Brovkin, P. Ciais, R. Fensholt, H. Tømmervik, G. Bala, Z. Zhu, R. R. Nemani, R. B. Myneni, China and India lead in greening of the world through land-use management. *Nat. Sustainability* **2**, 122–129 (2019).
42. H. Wei, Y. Zhang, Q. Huang, C. Liu, T. Wagener, Functional relationships reveal large differences in streamflow response to eCO_2-vegetation in global water models. *Geophys. Res. Lett.* **52**, e2024GL113685 (2025).
43. S. Gnann, R. Reinecke, L. Stein, Y. Wada, W. Thiery, H. Müller Schmied, Y. Satoh, Y. Pokhrel, S. Ostberg, A. Koutroulis, N. Hanasaki, M. Grillakis, S. N. Gosling, P. Burek, M. F. P. Bierkens, T. Wagener, Functional relationships reveal differences in the water cycle representation of global water models. *Nat. Water* **1**, 1079–1090 (2023).
44. A. J. Winkler, R. B. Myneni, G. A. Alexandrov, V. Brovkin, Earth system models underestimate carbon fixation by plants in the high latitudes. *Nat. Commun.* **10**, 885 (2019).
45. W. Li, M. Reichstein, S. O, C. May, G. Destouni, M. Migliavacca, B. Kraft, U. Weber, R. Orth, Contrasting drought propagation into the terrestrial water cycle between dry and wet regions. *Earth's Future* **11**, e2022EF003441 (2023).
46. S. Power, F. Delage, C. Chung, G. Kociuba, K. Keay, Robust twenty-first-century projections of El Niño and related precipitation variability. *Nature* **502**, 541–545 (2013).
47. Y. Liu, M. G. Donat, M. H. England, L. V. Alexander, A. L. Hirsch, C. Delgado-Torres, Enhanced multi-year predictability after El Niño and La Niña events. *Nat. Commun.* **14**, 6387 (2023).
48. Y. Liu, K. Duffy, J. G. Dy, A. R. Ganguly, Explainable deep learning for insights in El Niño and river flows. *Nat. Commun.* **14**, 339 (2023).
49. W. Brutsaert, M. B. Parlange, Hydrologic cycle explains the evaporation paradox. *Nature* **396**, 30–30 (1998).
50. M. L. Roderick, G. D. Farquhar, The cause of decreased pan evaporation over the past 50 years. *Science* **298**, 1410–1411 (2002).
51. Z. Yu, P. Ciais, S. Piao, R. A. Houghton, C. Lu, H. Tian, E. Agathokleous, G. R. Kattel, S. Sitch, D. Goll, X. Yue, A. Walker, P. Friedlingstein, A. K. Jain, S. Liu, G. Zhou, Forest expansion dominates China's land carbon sink since 1980. *Nat. Commun.* **13**, 5374 (2022).
52. P. Mehta, S. Siebert, M. Kummu, Q. Deng, T. Ali, L. Marston, W. Xie, K. F. Davis, Half of twenty-first century global irrigation expansion has been in water-stressed regions. *Nat. Water* **2**, 254–261 (2024).
53. J. Su, C. Miao, F. Zwiers, H. Beck, P. Jones, Q. Sun, L. J. Slater, W. R. Berghuijs, Y. Wada, D. Rosenfeld, J. Gou, Y. Wu, P. Tarolli, P. Borrelli, P. Panagos, L. V. Alexander, Q. Zhang, J. Hu, S.-K. Min, L. Samaniego, Q. Duan, G. Destouni, J. A. Marengo, R. Modarres, S. Sorooshian, Precipitation observing network gaps limit climate change impact assessment. *Nature* **652**, 119–125 (2026).
54. M. Mudelsee, Trend analysis of climate time series: A review of methods. *Earth-Sci. Rev.* **190**, 310–322 (2019).
55. N. Y. Krakauer, N. Devineni, Up-to-date probabilistic temperature climatologies. *Environ. Res. Lett.* **10**, 024014 (2015).
56. World Meteorological Organization, State of Global Water Resources report 2023 (WMO-No. 1362, 2024), pp. 1–69.
57. I. Harris, T. J. Osborn, P. Jones, D. Lister, Version 4 of the CRU TS monthly high-resolution gridded multivariate climate dataset. *Sci. Data* **7**, 109 (2020).
58. H. E. Beck, E. F. Wood, M. Pan, C. K. Fisher, D. G. Miralles, A. I. J. M. van Dijk, T. R. McVicar, R. F. Adler, MSWEP V2 global 3-hourly 0.1° precipitation: Methodology and quantitative assessment. *Bull. Am. Meteorol. Soc.* **100**, 473–500 (2019).
59. G. J. Huffman, R. F. Adler, A. Behrangi, D. T. Bolvin, E. J. Nelkin, G. Gu, M. R. Ehsani, The new version 3.2 Global Precipitation Climatology Project (GPCP) monthly and daily precipitation products. *J. Climate* **36**, 7635–7655 (2023).
60. B. D. Loomis, S. B. Luthcke, T. J. Sabaka, Regularization and error characterization of GRACE mascons. *J. Geod.* **93**, 1381–1398 (2019).
61. H. Save, S. Bettadpur, B. D. Tapley, High-resolution CSR GRACE RL05 mascons. *J. Geophys. Res. Solid Earth* **121**, 7547–7569 (2016).
62. F. W. Landerer, F. M. Flechtner, H. Save, F. H. Webb, T. Bandikova, W. I. Bertiger, S. V. Bettadpur, S. H. Byun, C. Dahle, H. Dobslaw, E. Fahnestock, N. Harvey, Z. Kang, G. L. H. Kruizinga, B. D. Loomis, C. McCullough, M. Murböck, P. Nagel, M. Paik, N. Pie, S. Poole, D. Strekalov, M. E. Tamisiea, F. Wang, M. M. Watkins, H.-Y. Wen, D. N. Wiese, D.-N. Yuan, Extending the global mass change data record: GRACE follow-on instrument and science data performance. *Geophys. Res. Lett.* **47**, e2020GL088306 (2020).
63. L. Wang, Y. Zhang, Filling GRACE data gap using an innovative transformer-based deep learning approach. *Remote Sens. Environ.* **315**, 114465 (2024).
64. S. Mo, Y. Zhong, E. Forootan, N. Mehrnegar, X. Yin, J. Wu, W. Feng, X. Shi, Bayesian convolutional neural networks for predicting the terrestrial water storage anomalies during GRACE and GRACE-FO gap. *J. Hydrol.* **604**, 127244 (2022).
65. A. Rateb, A. Sun, B. R. Scanlon, H. Save, E. Hasan, Reconstruction of GRACE mass change time series using a Bayesian framework. *Earth Space Sci.* **9**, e2021EA002162 (2022).
66. F. Li, J. Kusche, Reproducing GRACE total water storage change at finer spatial scales. *Geophys. Res. Lett.* **53**, e2025GL119881 (2026).
67. J. Gou, B. Soja, Global high-resolution total water storage anomalies from self-supervised data assimilation using deep learning algorithms. *Nat. Water* **2**, 139–150 (2024).
68. B. D. Richter, G. Lamsal, L. Marston, S. Dhakal, L. S. Sangha, R. R. Rushforth, D. Wei, B. L. Ruddell, K. F. Davis, A. Hernandez-Cruz, S. Sandoval-Solis, J. C. Schmidt, New water accounting reveals why the Colorado River no longer reaches the sea. *Commun. Earth Environ.* **5**, 134 (2024).
69. G. E. P. Box, G. Jenkins, *Time Series Analysis, Forecasting and Control* (Holden-Day, 1990).
70. Q. Mu, M. Zhao, S. W. Running, Improvements to a MODIS global terrestrial evapotranspiration algorithm. *Remote Sens. Environ.* **115**, 1781–1800 (2011).
71. B. Martens, D. G. Miralles, H. Lievens, R. van der Schalie, R. A. M. de Jeu, D. Fernández-Prieto, H. E. Beck, W. A. Dorigo, N. E. C. Verhoest, GLEAM v3: Satellite-based land evaporation and root-zone soil moisture. *Geosci. Model Dev.* **10**, 1903–1925 (2017).
72. N. Ma, J. Szilagyi, Y. Zhang, Calibration-free complementary relationship estimates terrestrial evapotranspiration globally. *Water Resour. Res.* **57**, e2021WR029691 (2021).
73. B. Lehner, G. Grill, Global river hydrography and network routing: Baseline data and new approaches to study the world's large river systems. *Hydrol. Process.* **27**, 2171–2186 (2013).
74. B. Lehner, K. Verdin, A. Jarvis, New global hydrography derived from spaceborne elevation data. *Am. Geophys. Union* **89**, 93–94 (2008).
75. W. J. Shuttleworth, "Evaporation," in *Handbook of Hydrology*, D. R. Maidment Ed. (McGraw-Hill, 1993), pp. 4.1–4.53.
76. M. Rodell, P. R. Houser, U. Jambor, J. Gottschalck, K. Mitchell, C.-J. Meng, K. Arsenault, B. Cosgrove, J. Radakovich, M. Bosilovich, J. K. Entin, J. P. Walker, D. Lohmann, D. Toll, The global land data assimilation system. *Bull. Am. Meteorol. Soc.* **85**, 381–394 (2004).
77. D. Kong, Y. Zhang, X. Gu, D. Wang, A robust method for reconstructing global MODIS EVI time series on the Google Earth Engine. *ISPRS J. Photogramm. Remote Sens.* **155**, 13–24 (2019).
78. F. Dominici, A. McDermott, S. L. Zeger, J. M. Samet, On the use of generalized additive models in time-series studies of air pollution and health. *Am. J. Epidemiol.* **156**, 193–203 (2002).
79. T. Portlock, T. Shama, S. H. Kakon, B. Hartjen, C. Pook, B. C. Wilson, A. Bhuttor, D. Ho, I. Shennon, A. M. Engelstad, R. Di Lorenzo, G. Greaves, N. Rahman, C. Kelsey, P. D. Gluckman, J. M. O'Sullivan, R. Haque, T. Forrester, C. A. Nelson, Interconnected pathways link faecal microbiota plasma lipids and brain activity to childhood malnutrition related cognition. *Nat. Commun.* **16**, 473 (2025).
80. Q. Feng, J. Shen, F. Yang, S. Liang, J. Liu, X. Kuang, D. Wang, Z. Zeng, Long-term gridded land evapotranspiration reconstruction using Deep Forest with high generalizability. *Sci. Data* **10**, 908 (2023).
81. R. M. O'brien, A caution regarding rules of thumb for variance inflation factors. *Qual. Quant.* **41**, 673–690 (2007).
82. M. A. Silva, C. Amado, D. Loureiro, Propagation of uncertainty in the water balance calculation in urban water supply systems – A new approach based on high-density regions. *Measurement* **126**, 356–368 (2018).

Acknowledgments: We appreciate the various water agencies stated in Materials and Methods for sharing the streamflow data. Our work was inspired by the preparation of the 2024 Annual Report of the WMO State of Global Water Resources. We thank the editor and the reviewers for the comments that helped improve this paper. **Funding:** Yongqiang Zhang acknowledges the National Natural Science Foundation of China (grant nos. 42361144709 and 42330506), and the Talent Program of the Ministry of Science and Technology of China. G.D. acknowledges support from the Swedish Research Council (VR, project grant 2022-04672).
Author contributions: Yongqiang Zhang conceived the study, wrote MATLAB scripts for data analysis and figures plotting, and drafted the paper. C.L. collated the streamflow dataset and conducted basin-water-balance analysis. D.K. collated CMIP6 and evapotranspiration datasets. Z.X. and C.L. prepared the attribution analysis dataset. H.W. plotted Fig. 5. All authors contributed to discussion, text revisions, and result interpretations. **Competing interests:** The authors declare that they have no competing interests. **Data, code, and materials availability:** All data and code needed to evaluate and reproduce the results in the paper are present in the paper and/or the Supplementary Materials. All data and code are available on Zenodo at https://zenodo.org/records/19914712. This study did not generate new materials.

Submitted 5 February 2026
Accepted 20 July 2026
Published 26 August 2026
10.1126/sciadv.aeg1633

Downloaded from https://www.science.org at Digitop - USDA's Digital Desktop Library on October 06, 2026

ScienceAdvances

Hemispheric asymmetry in evapotranspiration reveals terrestrial water-flux redistribution

Yongqiang Zhang, Congcong Li, Dongdong Kong, Zhenwu Xu, Diego Miralles, Tim R. McVicar, Jing Tian, Xuanze Zhang, Ning Ma, Xiaojie Li, Yongyong Zhang, Haoshan Wei, Gang Zhao, Jun Xia, Yuanyuan Huang, Zhipin Ai, Ronglin Tang, Ge Sun, Stefan Uhlenbrook, and Georgia Destouni

Sci. Adv. **12** (35), eaeg1633. DOI: 10.1126/sciadv.aeg1633

View the article online
https://www.science.org/doi/10.1126/sciadv.aeg1633
Permissions
https://www.science.org/help/reprints-and-permissions

Downloaded from https://www.science.org at Digitop - USDA's Digital Desktop Library on October 06, 2026

Use of this article is subject to the Terms of service

Science Advances (ISSN 2375-2548) is published by the American Association for the Advancement of Science. 1200 New York Avenue NW, Washington, DC 20005. The title *Science Advances* is a registered trademark of AAAS.

Copyright © 2026 The Authors, some rights reserved; exclusive licensee American Association for the Advancement of Science. No claim to original U.S. Government Works. Distributed under a Creative Commons Attribution NonCommercial License 4.0 (CC BY-NC).